

## Protein Structural Denaturation Evaluated by MCR-ALS of Protein Microarray FTIR Spectra

Joëlle De Meutter and Erik Goormaghtigh\*

Cite This: *Anal. Chem.* 2021, 93, 13441–13449

Read Online

ACCESS |



Metrics &amp; More

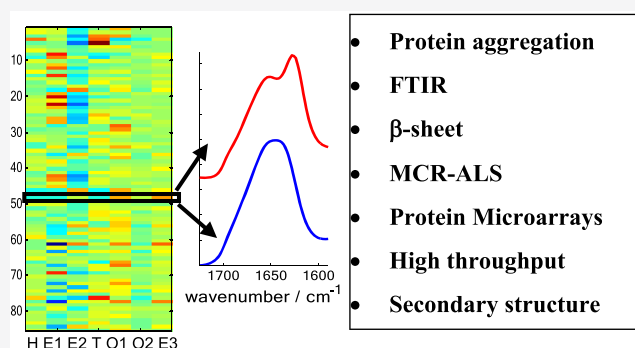


Article Recommendations



Supporting Information

**ABSTRACT:** The loss of native structure is common in proteins. Among others, aggregation is one structural modification of particular importance as it is a major concern for the efficiency and safety of biotherapeutic proteins. Yet, recognizing the structural features associated with intermolecular bridging in a high-throughput manner remains a challenge. We combined here the use of protein microarrays spotted at a density of ca 2500 samples per  $\text{cm}^2$  and Fourier transform infrared (FTIR) imaging to analyze structural modifications in a set of 85 proteins characterized by widely different secondary structure contents, submitted or not to mild denaturing conditions. Multivariate curve resolution alternating least squares (MCR-ALS) was used to model a new spectral component appearing in the protein set subject to denaturing conditions. In the native protein set, 6 components were found to be sufficient to obtain good modeling of the spectra. Furthermore, their shape allowed them to be assigned to  $\alpha$ -helix,  $\beta$ -sheet, and other structures. Their content in each protein was correlated with the known secondary structure, confirming these assignments. In the denatured proteins, a new component was necessary and modeled by MCR-ALS. This new component could be assigned to the intermolecular  $\beta$ -sheet, bridging protein molecules. MCR-ALS, therefore, unveiled a potential spectroscopic marker of protein aggregation and allowed a semiquantitative evaluation of its content. Insight into other structural rearrangements was also obtained.



Proteins are widely used as commercial biotechnological products in research laboratories as well as food and Biopharma industries. Biotherapeutics (i.e., antibodies, hormones, and enzymes) constitute one of the fastest-growing classes among therapeutic actors to treat various cancers, autoimmune diseases, or metabolic disorders as well as to prevent infectious diseases (vaccines).<sup>1</sup> The preservation of the protein native conformation is a major concern due to its intrinsic instability. The loss of native structure is a common response to chemical or physical stresses such as temperature, pH, co-solutes, and adsorption onto interfaces. It can occur from production, purification, transport, and delivery to the patient. Altered structures of proteins have a strong tendency to self-associate in assemblies (aggregates). Protein aggregates can reduce the effectiveness of drugs but can also increase their immunogenicity with dramatic consequences. As there is a strong correlation between aggregation and immunogenicity, it has been suggested that aggregation could be used as a predictor for immunogenicity of Biotherapeutics.<sup>2</sup> Conformational stability is, therefore, a major concern as even a small percentage of aggregate molecules can lead to undesirable effects.<sup>3</sup> The majority of protein formulations contains a low level of aggregates, although the extent and type of aggregation that could represent a risk is still a matter of debate.<sup>4</sup> Pharmacopoeias have established limits of tolerance for

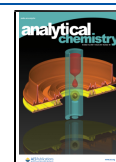
aggregates in formulations and tedious screening is performed all along the production lines.<sup>5</sup>

As recently reviewed,<sup>6</sup> Fourier transform infrared (FTIR) spectroscopy is a powerful technique to determine the conformation of proteins in native<sup>7–9</sup> and unfolded or aggregate states, for instance in amyloid structures.<sup>10–12</sup> It is reported in the literature that FTIR spectroscopy has the potential to differentiate between different types of native secondary structures and even different types of aggregates.<sup>12–16</sup> In native globular proteins,  $\beta$ -sheet bands below  $1630 \text{ cm}^{-1}$  are rare.<sup>17</sup> Upon aggregation of monoclonal antibodies, Baird et al.<sup>18</sup> identified a protein conformation characterized by  $\beta$ -sheet spectral features but absorbing at lower wavenumbers. The intramolecular  $\beta$ -sheet peak found at  $1639 \text{ cm}^{-1}$  in the native protein shifted to  $1625 \text{ cm}^{-1}$ . Devi et al.<sup>19</sup> also measured thermal unfolding curves of high concentrations of bovine IgG by FTIR, revealing intermo-

Received: April 2, 2021

Accepted: August 3, 2021

Published: September 30, 2021



lecular  $\beta$ -sheets absorbing at 1625 and 1692  $\text{cm}^{-1}$ . Militello et al. demonstrated that a new band appears near 1615  $\text{cm}^{-1}$  in bovine serum albumin when exposed at 58 °C at pH 7.4.<sup>20</sup> The presence of these absorption bands at lower wavenumbers is indicative of stronger H bonds, suggesting that intermolecular interactions that lead to aggregation involve  $\beta$ -strands with stronger H bonds than those found in native-like structures.<sup>13</sup> While such contribution has been described in a number of proteins, an overview on a large protein panel is still missing.

Another challenge is to deal with the high number of samples from production lines or from studies including a high number of environmental conditions such as generated by thermal or mechanical stress studies, freeze–thaw cycles, shaking, etc. Kazarian and colleagues have introduced an attenuated total reflection (ATR) FTIR spectroscopy approach to monitor protein aggregation in situ.<sup>6,21</sup> Using macro ATR-FTIR imaging, 12 different samples can be monitored simultaneously. While the crucial advantage of the approach is the possibility to perform monitoring in situ, during a temperature ramp, for instance, the number of samples remains limited. To tackle the high-throughput problem, we recently introduced a new method specifically designed for high-throughput protein structure determination, combining microarrays of proteins spotted at a density of ca 2000–4000 samples per  $\text{cm}^2$  and FTIR imaging.<sup>8,22,23</sup> The secondary structure of a protein is usually obtained by chemometric methods, including on protein microarrays.<sup>8,24–26</sup> Adequate calibration is obtained using a large set of proteins designed to cover the protein structural space, both in terms of secondary structures and higher-level structures. Such a recently developed protein set is cSP92, which contains 92 well-characterized proteins.<sup>27</sup> Yet, structural features induced in the course of protein denaturation may not be present in native proteins used for calibration, limiting the usefulness of regular chemometric approaches. The multivariate techniques, typically used for protein secondary structure evaluation, cannot address appropriately the issues raised by the appearance, in denatured proteins, of unconventional structures that do not exist in crystallized proteins. Indeed, upon aggregation, proteins form a wide diversity of assemblies, which do not crystallize, precluding the use of X-ray crystallography. As, in general, neither NMR nor cryogenic electron microscopy (cryo-EM) can tackle efficiently such a situation, no adequate calibration is possible.

Multivariate curve resolution (MCR) is a soft-modeling technique designed to solve the bilinear description of the data in terms of both spectra of “pure” components and their related concentrations, potentially in the absence of knowledge about the spectral shape of the pure components. Unlike principal component analysis (PCA), there is an infinity of solutions for MCR. The problem is alleviated by the introduction of constraints such as the nonnegativity for the concentrations and spectral profiles.<sup>28–30</sup> Alternating least-squares MCR (MCR-ALS) iteratively solves the problem using these constraints and others as reviewed elsewhere.<sup>31</sup> Numerous examples of applications of MCR-ALS in chemistry, biology, and pharmaceutical sciences have been published. MCR-ALS was applied to detect intermediate structures in protein folding monitored by circular dichroism (CD) spectroscopy.<sup>32</sup> It was also used to obtain pure spectral and concentration profiles in the course of the transition between  $\alpha$ -helices and  $\beta$ -intermolecular  $\beta$ -sheets in poly-L-lysine solution at varying pH conditions and across a wide range of

concentrations.<sup>33</sup> An attempt to resolve the protein secondary structure from a 24 protein FTIR spectral database was presented.<sup>34</sup> The most relevant feature of MCR is that it provides meaningful models without a priori information on the system itself, giving component spectral profiles with a chemical sense.

In the present work, we address the issue of protein denaturation/aggregation by MCR-ALS. In one protein set, we have only native structures. In the second one, the same proteins have been exposed to a mild detergent, dodecylphosphocholine (DPC), which induces structural modifications in some of them. A wide diversity of proteins was tested using the protein microarray approach. We proceeded in three steps. In a first step, the MCR component profiles describing the native protein structural component spectra were obtained. They were carefully characterized to establish their structural significance with regard to the reference structural content available for these native proteins. In a second step, we observed that MCR could put forward the presence of structural changes in some of the proteins exposed to DPC. Yet, it appeared that a simple readjustment of the concentrations of the classical structures found in native proteins was not sufficient. The quality of the fit for the denatured protein spectra was indeed much poorer than for the native proteins. In a third step, we used MCR-ALS to model an additional component that was revealed to be a type of  $\beta$ -sheet structure not present in native proteins but described in the literature as belonging to intermolecular  $\beta$ -sheets typically involved in protein aggregation. MCR, therefore, unveiled a potential spectroscopic marker of protein aggregation and allowed a semiquantitative evaluation of its content.

## 1. EXPERIMENTAL SECTION

**1.1. Proteins.** The 92 protein set belongs to cSP92, a protein library recently designed for spectroscopic calibrations.<sup>27</sup> Denaturation of the proteins was induced by the addition of deuterated dodecylphosphocholine-d38 (DPC) (final concentration: 5 mg/mL) to the 92 protein samples in a solution containing 50% v/v ethylene glycol (EG). The simultaneous presence of both EG and DPC induced an alteration of secondary structure in some proteins. DPC was acquired from Sigma-Aldrich.

**1.2. Microarray Printing-Imaging.** The formation of both protein microarrays and microarray FTIR imaging have been described in detail previously,<sup>8</sup> and are summarized in the Supporting Information (SI). Briefly, proteins at a final concentration of 10–20 mg/mL were buffer-exchanged against 4 mM HEPES, 85 mM NaCl (5%), at pH between 7.4 and 7.6, if not otherwise specified.<sup>27</sup> A 2-fold dilution occurred after the addition of EG and 4-fold when DPC was added. After spotting, EG and water were removed under a mild vacuum. The spectra were recorded as the average of 64 scans, between 3650 and 900  $\text{cm}^{-1}$  at a nominal resolution of 8  $\text{cm}^{-1}$ . FTIR data were collected using an Agilent mid-IR imager equipped with a liquid-nitrogen-cooled 128  $\times$  128 mercury cadmium telluride (MCT) focal plane array (FPA) detector and a 15 $\times$  objective (NA = 0.62). The corresponding pixel covers an area of 5.5  $\times$  5.5  $\mu\text{m}^2$ . Data were finally encoded every 1  $\text{cm}^{-1}$  by linear interpolation. The background image (128 scans per pixel) was acquired in the absence of the sample on a clean surface of a BaF<sub>2</sub> slide. When DPC was present, even though not absorbing in the amide I spectral range, its contribution

was subtracted after scaling on the integrated absorbance peak of the  $\nu(\text{C}=\text{H})$  between 2250 and 2044  $\text{cm}^{-1}$ . The reproducibility of the spectral shape among quadruplicate experiments is illustrated in Figure S1.

**1.3. MCR-ALS.** Multivariate curve resolution-alternating least squares (MCR-ALS)<sup>28,31,35,36</sup> is a method widely used to resolve the problems of multicomponent mixtures. In spectroscopy, according to the Beer law, spectra of a mixture are a weighted sum of the spectra of each pure component. Equation 1 is the multi-wavelength extension of Lambert–Beer's law in a matrix format **D**, containing the spectra row-wise, can be decomposed into a concentration matrix **C** and a spectrum matrix **S**.

$$\mathbf{D} = \mathbf{CS}^T + \mathbf{E} \quad (1)$$

The concentrations (or contributions) of the pure species present in the chemical system are reported in the columns of **C** and the corresponding pure spectra in the rows of **S**.  $\mathbf{S}^T$  is the transpose of **S**. The matrix **E** contains the residuals not explained by the model. An infinity of solutions exists for the couple **C** and  $\mathbf{S}^T$  that can rebuild the data matrix **D** efficiently (rotational ambiguity).<sup>35</sup> MCR not only targets the smallest residuals but also a chemically meaningful result, i.e., pure spectra representing the actual components of the system. In an attempt to ease the rotational ambiguity problem, MCR-ALS adds, as constraints, any information that is known on the system. In the present work, the obvious information to be added is that neither the pure spectra nor the concentrations can be negative though a 5% tolerance is allowed for the spectral profiles.<sup>35,36</sup> It can also be added that the sum of the concentrations must be 100%. An a priori selection of the most relevant information contained in the data set is needed to initiate the iterative MCR-ALS process. SIMPLE-to-use Interactive Self-modeling Mixture Analysis (SIMPLISMA)<sup>37,38</sup> was used here to identify the most dissimilar spectra of the data set, which are of interest as initial estimates. Starting with the initial estimates for  $\mathbf{S}^T$ , an iterative algorithm (ALS) solves eq 1 for the concentration matrix **C** under the direction of appropriate constraints. Once an estimate of **C** is obtained with the constraints applied, eq 1 is solved for  $\mathbf{S}^T$ , under the constraints described above for  $\mathbf{S}^T$ . The optimization process is repeated until the model  $\mathbf{CS}^T$  reproduces the experimental data matrix **D** satisfactorily according to a convergence criterion. At each step, the error matrix  $\mathbf{E} = \mathbf{D} - \mathbf{CS}^T$  is evaluated. In practice, convergence is achieved when the relative decrease in the standard deviation of the residuals between two consecutive iterative cycles,  $\sigma$ , is less than a threshold value, usually 0.1%.  $\sigma$  is defined as

$$\sigma = \sqrt{\frac{\sum_{i,j} e_{ij}^2}{n_{\text{rows}} n_{\text{columns}}}} \quad (2)$$

where  $e_{ij}$  are the elements of the error matrix **E**,  $n_{\text{rows}}$  is the number of rows (number of spectra) in the data matrix **D**, and  $n_{\text{columns}}$  is the number of columns (number of data points in a spectrum) in **D**. While the absolute value of  $\sigma$  depends on the units, a more general evaluation of the quality of the optimization procedure and fitting can be obtained as the percent of lack of fit (% LOF).

$$\text{LOF} = 100 \sqrt{\frac{\sum_{i,j} e_{ij}^2}{\sum_{i,j} d_{ij}^2}} \quad (3)$$

where  $d_{ij}$  are the elements of the data matrix **D**. Finally,  $\sigma$  from MCR-ALS ( $\sigma_{\text{MCR}}$ ) can be compared with  $\sigma_{\text{PCA}}$  obtained similarly after reconstruction of **D** with the same number of principal components obtained by principal component analysis (PCA). PCA will provide the lowest possible value of  $\sigma$  for a given number of components.

Image analysis, spectrum processing, and multivariate analyses were all performed with Kinetics, the home-made software running under MatLab (The MathWorks Inc.).

## 2. RESULTS

The first step in this work consisted of identifying the spectral contributions of pure component profiles present in the native protein spectra that can be retrieved by MCR-ALS. Infrared images of the microarrays were recorded for the 92 proteins of the cSP92 protein library.<sup>27</sup> This set of 92 spectra constitutes the **D**<sub>192</sub> matrix described hereafter. The spectra are presented in Figure 1 in the amide I spectral region, i.e., an absorption

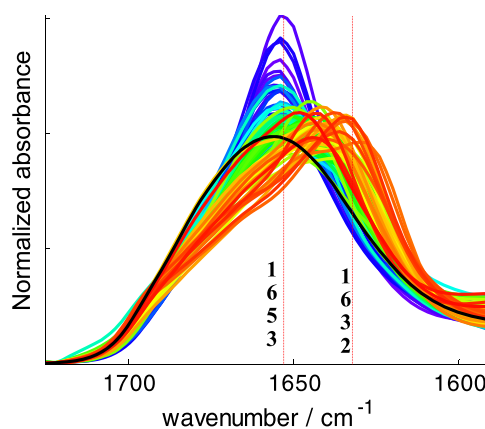


**Figure 1.** FTIR protein spectra of the cSP92 protein set. Vertical lines indicate the position of a typical  $\alpha$ -helix maximum around 1653  $\text{cm}^{-1}$  and a low limit position for  $\beta$ -sheets at 1632  $\text{cm}^{-1}$  as discussed in the text. Spectra are sorted in the descending order of the  $\alpha$ -helix content and color evolves from blue to red.

band originating mostly from the amide  $\nu(\text{C}=\text{O})$ . For proteins, this band contains most structural information than can be retrieved from infrared spectra.<sup>7–9,39</sup> It can be observed in Figure 1 that each protein has a different spectrum.

The diversity of the spectral shapes is not only related to the various contents in secondary structures but also to the fine variations of the geometry of these structures.<sup>40–42</sup> In Figure 1, proteins have been sorted according to the helix content. The color evolves from blue to red: the highest  $\alpha$ -helix content protein spectra are drawn in blue and the lowest  $\alpha$ -helix content protein spectra in red. The  $\alpha$ -helix contribution can be observed around 1653  $\text{cm}^{-1}$ . As there is a marked anticorrelation between  $\alpha$ -helix and  $\beta$ -sheet content,<sup>27</sup> red spectra belong to proteins rich in  $\beta$ -sheets. While the most  $\alpha$ -helix contributions appear around 1653  $\text{cm}^{-1}$ , the spread of the peak positions is much larger for the  $\beta$ -sheet. It is found in a range between 1640 and 1632  $\text{cm}^{-1}$ . The low wavenumber limit for native  $\beta$ -sheet is 1632  $\text{cm}^{-1}$  in **D**<sub>192</sub>, as indicated in the figure. Only one protein is found below this limit. The black spectrum in Figure 1 belongs to metallothionein, an intrinsically disordered protein. It is characterized by a broadband centered around 1656  $\text{cm}^{-1}$ .

**2.1. MCR Pure Component Spectral Profiles Present in Native Protein Spectra.** As indicated in the Experimental Section, MCR-ALS requires both a starting point for  $S^T$  and an evaluation of the number of components. To evaluate the number of components, we found that the usual techniques such as singular-value decomposition (SVD)<sup>29</sup> could not provide a clear answer. We therefore manually varied the number of components from 3 to 7. We concluded that the optimum was 6 components on the basis of the correlation of the MCR profile contents with the actual secondary structure content, as will be described later. Results for 6 components are therefore presented here. To identify the starting point for  $S^T$ , we applied the SIMPLISMA algorithm (see the Experimental Section). SIMPLISMA provides initial estimates representing the  $n$  most different spectra of the set. Running MCR-ALS resulted in 6 MCR profiles presented in Figure 2A.

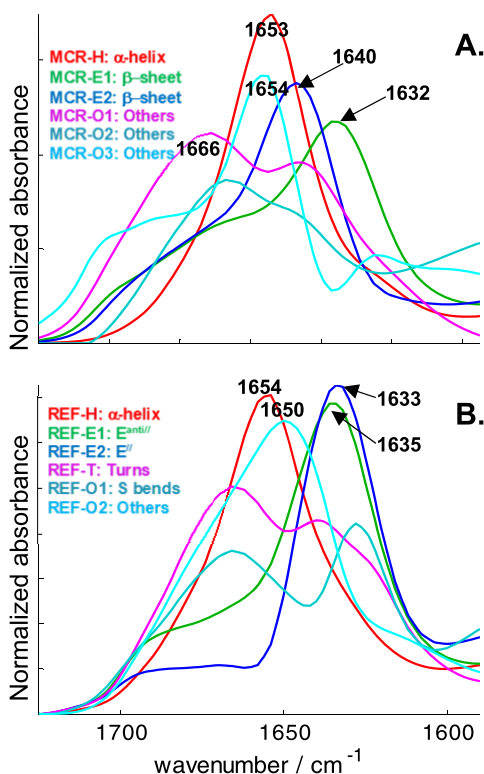


**Figure 2.** (A) Six MCR-ALS component profiles obtained from the DI<sub>92</sub> database; inset: tentative assignments of MCR profiles to secondary structure elements. (B) The shape of the reference profiles for 6 structural elements defined by DSSP that contribute to the spectra of DI<sub>92</sub>. The C matrix contained the concentration in H, E<sup>anti//</sup>, E<sup>//</sup>, T, S, and O for each protein. Assignments are reported in the inset of panel (B).

In Figure 2A, the first MCR component has a maximum located at 1653 cm<sup>-1</sup> and could be tentatively assigned to the  $\alpha$ -helix structure (H). It is therefore labeled MCR-H. The next 2 MCR components have a maximum at 1632 and 1640 cm<sup>-1</sup>, respectively, as well as a shoulder near 1690 cm<sup>-1</sup>, i.e., spectral features characteristic of  $\beta$ -sheets (E) as reviewed in the literature.<sup>17,39,43</sup> They are labeled MCR-E1 and MCR-E2, respectively. The 3 remaining profiles could not be assigned to any well-defined structure. They presumably belong to the so-called “random” structures. They are identified in this work as MCR-O1, MCR-O2, and MCR-O3, with “O” standing for “Others”.

**2.2. Validation of Structural Assignments of MCR Profiles Present in Native Protein Spectra.** The tentative assignment of the MCR profiles to different secondary structures presented in Figure 2A can be confirmed as high-resolution structures of the proteins and are available in the protein data bank (PDB).<sup>44</sup> The three-dimensional (3D) structures in the PDB need to be analyzed to identify and quantify the secondary structure elements such as the  $\alpha$ -helix and  $\beta$ -sheet. Several definitions used to quantify these secondary structure elements are available. The most widely used, the DSSP algorithm,<sup>45</sup> was also found to provide the secondary structure content well related to the FTIR spectra,<sup>25</sup> and will be used in this work. DSSP identifies 8 secondary structures:  $\alpha$ -helix (H),  $\beta$ -sheet (E), 3<sub>10</sub> helix (G),  $\pi$ -helix (I), helix-turns (T),  $\beta$ -bridge (B), and bends (S). The remaining residues are assigned to others (O). The more usual terminology “random” could be used but, depending on the definitions, the random structure also includes some of the turns, bends, and less frequent structures, resulting in a confusing definition of the random category. The  $\beta$ -sheet structure can, in turn, be divided into “parallel” (E<sup>//</sup>) and “antiparallel” (E<sup>anti//</sup>)  $\beta$ -sheet, which may have distinct FTIR spectra, at least in amyloid-forming proteins.<sup>10–12,46</sup> All these structural features present in the cSP92 protein set have been described and tabulated previously.<sup>27</sup>

**2.2.1. Comparison of MCR Profiles with Spectral Profiles Obtained from the Known DSSP-Defined Concentrations.** As the secondary structure contents are known from the DSSP analysis of the high-resolution structures deposited in the PDB, eq 1 can be solved to retrieve S, i.e., the reference spectral profile of these structures. The C matrix in eq 1 contains, therefore, the DSSP-derived secondary structure contents. Extracting S using C makes sense only if the variability in each secondary structure content is sufficient. Only 6 structural elements have a standard deviation value exceeding 4%:  $\alpha$ -helix (H), antiparallel  $\beta$ -sheet (E<sup>anti//</sup>), parallel  $\beta$ -sheet (E<sup>//</sup>), turns (T), bends (S), and others (O) (Table S1). It must be noted that some amino acid side chains (LYS, ARG, GLN, ASN) also absorb in the amide I spectral region<sup>47,48</sup> Yet, the associated standard deviation is always below 4% and their contributions affect the evaluation of secondary structure content only very moderately.<sup>26</sup> They were not further considered. Six reference profiles were therefore calculated for H, E<sup>anti//</sup>, E<sup>//</sup>, T, S, and O contents. The calculated spectral contributions appear as in Figure 2B. Comparing the shape of the spectra presented in Figure 2A (MCR profiles) and Figure 2B (reference profiles), one can notice a similarity for the first 3 of them even though the reference profiles for E<sup>anti//</sup> and E<sup>//</sup> show similar amide I maximum (around 1632 cm<sup>-1</sup>) suggesting that the two variants of the  $\beta$ -sheet could not be clearly delineated. It was indeed demonstrated that quantification of E<sup>anti//</sup> and E<sup>//</sup> structures individually remains difficult on the basis of the cSP92 spectral library.<sup>8</sup> We, therefore, preferred to assign MCR-E1 and MCR-E2 to two forms of  $\beta$ -sheets, without reference to the parallel or antiparallel type.

**2.2.2. Comparison of the MCR Component Content with DSSP Reference Values.** A more quantitative approach to validate the assignment of the MCR components to specific secondary structures would consist of comparing, for all proteins, the content in each MCR component with the content in DSSP-defined structures. The 2  $\beta$ -sheet structures represented by 2 MCR profiles have been pooled for the purpose of comparison. Such an approach was followed for

Table 1. Characterization of MCR-ALS Applied to D1<sub>92</sub> for 3–7 Components as Indicated in the First Column<sup>a</sup>

MCR-ALS	% LOF	$\beta$ -sheet				$\alpha$ -helix			
		$N^{\text{MCR}}$	$R$	RMSE	$\zeta$	$N^{\text{MCR}}$	$R$	RMSE	$\zeta$
3 comp	4.50	1	0.89	6.34	2.16	1	0.78	11.05	1.65
4 comp	3.60	2	0.89	6.2	2.21	1	0.90	8.01	2.28
5 comp	2.61	2	0.89	6.2	2.21	1	0.89	8.2	2.23
6 comp	2.37	2	0.89	6.32	2.17	1	0.90	8.12	2.25
7 comp	2.09	3	0.88	6.44	2.13	1	0.88	8.82	2.07
		2	0.87	6.83	2	3	0.91	7.47	2.45

<sup>a</sup>The overall lack-of-fit (LOF) is reported in the second column. The correlations between the abundance of MCR components and the DSSP-defined secondary structures  $\beta$ -sheet and  $\alpha$ -helix are characterized by the correlation coefficient  $R$ , root mean square error of prediction (RMSEP), and  $\zeta$ . The correlation was computed for 1 MCR component or the sum of 2 or 3 of them (Table S2). The number of components yielding the best  $R$  is reported under  $N^{\text{MCR}}$ .

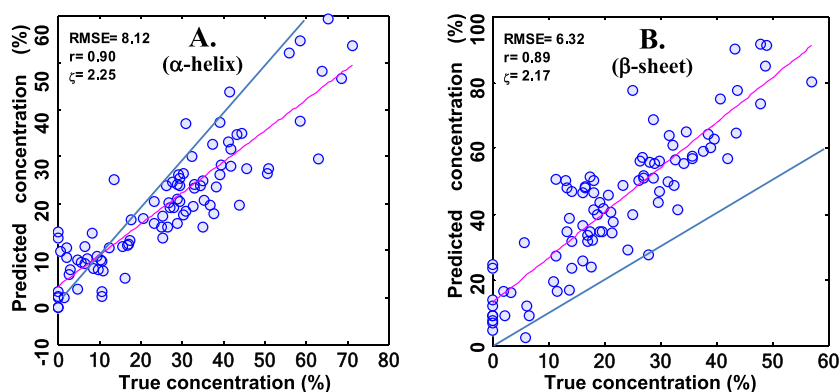


Figure 3. Relation between the predicted  $\alpha$ -helix (A) and  $\beta$ -sheet (B) structure contents (%) obtained for MCR components and the actual (“true”) secondary structure content obtained after analysis of PDB-stored high-resolution structure by DSSP. All concentrations are reported in %. Each circle in the graph represents a protein. The root mean square error (RMSE), correlation coefficient  $r$ , and  $\zeta$  are given in the figure. The regression line is colored in red while the diagonal is colored in blue.

MCR profiles obtained for 3–7 components. The results are reported in Table 1 for the  $\beta$ -sheet and  $\alpha$ -helix structures. The correlation coefficients between the DSSP-defined H content and MCR-H content are found to be between 0.78 and 0.91. Between the DSSP-defined E content and MCR-E content, the correlation coefficients are between 0.87 and 0.89. For each DSSP-derived secondary structure, the correlation with the content in each MCR profile taken individually and a combination of 2 or 3 of them was analyzed (Table S2 for 6 components). Only the highest correlations are reported in Table 1.

The correlation is better appreciated in terms of the usual secondary structure evaluation metrics, i.e., considering the linear relationship between MCR component contents and the secondary structure content as a tool for secondary structure prediction (Figure 3). In this context, the root mean square error of prediction (RMSEP) and  $\zeta$ , the ratio between the standard deviation of the structure content (Table S1), and the RMSEP,<sup>7,24,49</sup> are reported in Table 1. Table 1 indicates that  $\zeta$  varies between 2.0 and 2.21 for  $\beta$ -sheets and 1.65 and 2.45 for  $\alpha$ -helix. For the sake of the comparison, when fitting the experimental spectra by the 6 reference profiles obtained using the known concentration in  $\alpha$ -helix (reported in Figure 2B), the RMSE is 9.42% and  $\zeta = 1.88$ , indicating that the MCR-ALS spectral profiles are even better related to secondary structure content. As reported in Table 1 for 3–7 MCR components, the LOF varies from 4.50% for 3 components to 2.09% for 7. When selecting the number of components, it must be kept in mind that a sufficient number of components must be selected

to obtain a good description of the experimental D matrix. If the description is too approximate, the analysis of variations related to potential protein denaturation will be blurred by the large LOF already present. In particular, if new structures, unknown in the original data set, are formed, the LOF already present in the model will compete in the fitting with the additional LOF created by the appearance of the new component. Considering this problem, 6 components were retained. This number is, furthermore, in line with the observation that the LOF decay rate markedly decreases between 5 and 6 components (Figure S2A). Simultaneously, the difference between  $\sigma_{\text{MCR}}$  and  $\sigma_{\text{PCA}}$  starts increasing (Figure S2B) and correlation with the  $\beta$ -sheet content starts decreasing (Figure S2C). The values reported in Table 1 also indicate that adding a seventh component improves the correlation with the  $\alpha$ -helix, though only when described as the sum of 3 MCR components but degrades the correlation with the  $\beta$ -sheet content. Altogether, 6 components appeared to be a natural choice.

It is interesting to examine in more detail the relation between actual (DSSP) and estimated (MCR) contributions in the proteins. Figure 3A reports this comparison for the  $\alpha$ -helix and Figure 3B for the  $\beta$ -sheet content. It must be noted that, for the  $\beta$ -sheet, contributions of the MCR-E1 and E2 components were summed up as indicated in Table 1.

The RMSE values are 8.12 and 6.32% for the  $\alpha$ -helix and  $\beta$ -sheet, respectively. It can be observed that the slope of the line is less than 45° in the case of  $\alpha$ -helix and slightly higher than 45° for the  $\beta$ -sheet. Though this does not decrease the quality

of the correlation, it indicates that the MCR-H component identifies fewer amide groups and the MCR-E1 + MCR-E2 identifies more amide groups than the corresponding DSSP definitions. This is not unexpected as large differences in the secondary structure content can result from the application of different secondary structure definitions to the same set of 3D coordinates found in the PDB.<sup>25</sup> Furthermore, structurally distinct protein segments whose concentration covaries with H or E content cannot be resolved by MCR. Figure 3, therefore, sheds light on how FTIR naturally segments the DSSP-defined structural components.

**2.3. Proteins with Potential Denaturation.** From the 92 proteins of cSP92 exposed to DPC and EG, only 85 (Table S3) presented FTIR spectra of sufficient quality, i.e., passing the signal-to-noise threshold set for retaining the spectra.<sup>25</sup> The reason for the loss of quality was either the dilution of the solutions or the loss of materials following massive aggregation. A subset of the  $D1_{92}$  matrix, called  $D1_{85}$ , was therefore built to match the data obtained on the 85 proteins exposed to DPC, called  $D2_{85}$ .

**2.3.1. Fit with Previously Identified MCR Profiles.** In a first attempt,  $D2_{85}$  was fitted with the MCR components describing the native protein spectra (Figure 2A). A reorganization of the MCR profile contents was expected to provide a quantitative evaluation of the structural changes, if any. Yet, it was found that the LOF was more than doubled (4.97% instead of 2.25%), indicating that the previously obtained MCR components were not sufficient to describe correctly the proteins present in  $D2_{85}$ . This strongly suggests that unconventional structures, not found in the native proteins, appeared upon exposure to DPC and EG.

**2.3.2. Addition of a New MCR Component.** A close visual inspection of the spectrum series after Fourier self-deconvolution reveals that some proteins of  $D2_{85}$  have an absorbance band below  $1632\text{ cm}^{-1}$ . Figure 4A shows deconvolved spectra of  $D1_{85}$  and Figure 4B shows those of  $D2_{85}$ . We clearly see an increase in structures absorbing around  $1623\text{ cm}^{-1}$ . The difference spectra ( $D2_{85}-D1_{85}$ ) also indicate that, globally, an increased absorbance occurs around  $1623\text{ cm}^{-1}$  at the expense of absorbance found around  $1640\text{ cm}^{-1}$  (Figure S3).

In an attempt to account for the new structure present in  $D2_{85}$ , an additional MCR component was selected by SIMPLISMA and added to the MCR-ALS procedure. The additional initial component is colored in black in Figure 4B (after Fourier self-deconvolution, see the SI). As the goal was to analyze the new component, the shape of the first six ones was constrained to remain unchanged in the MCR-ALS analysis. Non-negativity constraints on both spectra and concentrations and a sum of 100% for all concentrations were applied as before. The MCR-ALS process, therefore, adjusted the concentration of all seven components but modeled both the shape and the concentration for only the seventh one. The new 7th component profile obtained appears in dark green in Figure 5B. As it has all the characteristics of a  $\beta$ -sheet spectrum, though with a maximum at an unusually low wavenumber, it was called MCR-E3.

Figure 5A compares the second derivative of MCR-E1, E2, and E3, i.e., the profiles assigned to different forms of the  $\beta$ -sheet. The maximum absorbance peaks, located at  $1640$  (MCR-E1),  $1632$  (MCR-E2), and  $1623\text{ cm}^{-1}$  (MCR-E3), with a shoulder around  $1690\text{ cm}^{-1}$ , were clearly defined on second-derivative spectra.

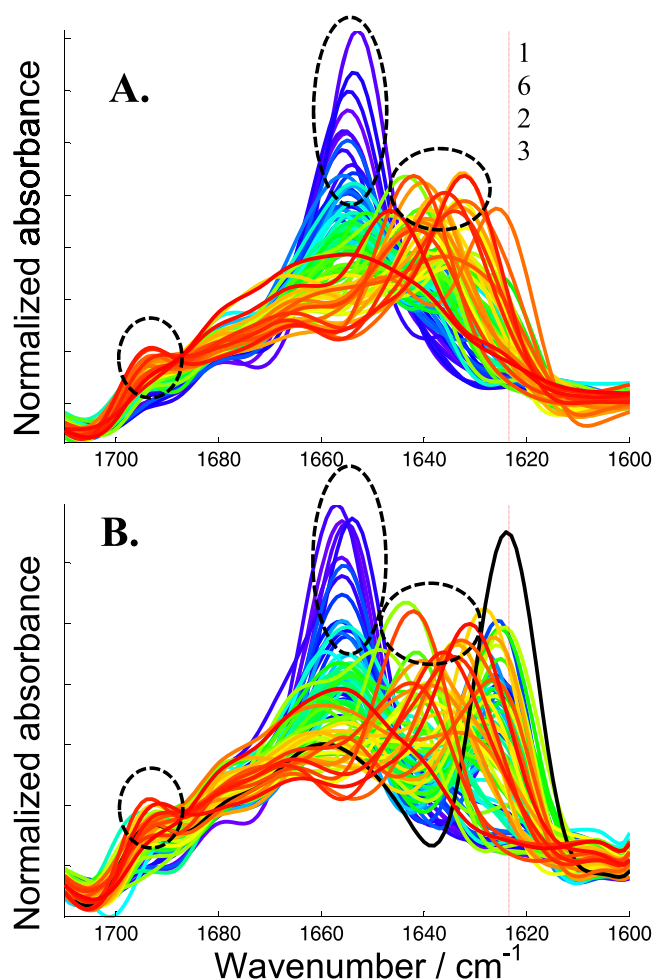


**Figure 4.** Eighty-five deconvolved spectra of proteins of  $D1_{85}$  (A) and  $D2_{85}$  (B). Spectra were sorted by decreasing the  $\alpha$ -helix content. Colors follow a scale from blue to red. In red:  $\beta$ -sheet rich proteins ( $1642\text{--}1630\text{ cm}^{-1}$ ); in blue:  $\alpha$ -helix rich proteins ( $1652\text{--}1656\text{ cm}^{-1}$ ).

### 3. DISCUSSION

Evidencing structural changes in proteins by FTIR spectroscopy is easily obtained by spectral comparisons. Relating the spectral changes to meaningful secondary structures is much less obvious, especially when these structures are unknown in libraries of proteins in their native structural state. MCR-ALS offers a decomposition of the spectra into a series of structurally meaningful components. In this work, we compared a series of proteins in their native structural state with the same proteins exposed to a mild zwitterionic detergent, DPC, in the presence of EG, an additive required for printing protein microarray that can be easily removed by evaporation. Interestingly, neither DPC nor EG alone was able to induce structural modifications in the protein set. It was indeed shown previously that when the FTIR spectra of all of the proteins from cSP92 were recorded both in protein microarrays, thus including the addition of EG, and by attenuated total reflection (ATR) FTIR in the absence of EG, no structural change was revealed.<sup>8</sup> Similarly, ATR spectra of the proteins recorded in the presence of DPC alone did not reveal protein denaturation either (unpublished). Even though DPC has been by far the most widely used detergent in solution-NMR, it has been reported by Kurauskas et al. that it may produce nonfunctional proteins.<sup>50</sup> In this work, when

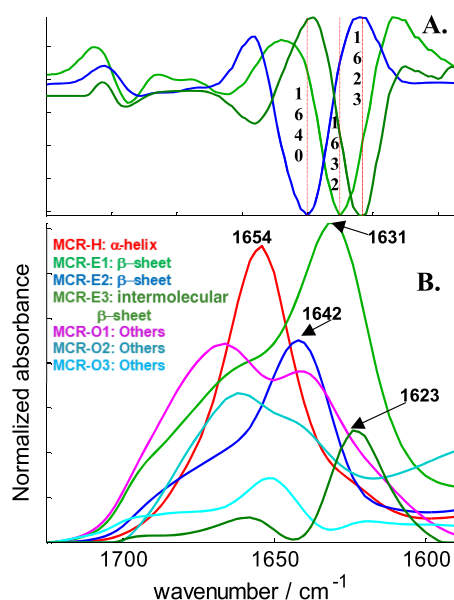


**Figure 5.** (A) Second derivatives of the 3 MCR components assigned to  $\beta$ -sheet structures presented in panel (B). (B) MCR-ALS analysis of  $\text{D}_{285}$  with a seventh component added (dark green). For the sake of readability, the components have been multiplied by their mean content in  $\text{D}_{285}$ .

DPC and EG were taken together, some proteins were destabilized and experienced structural changes. Understanding the reasons for the conjugated effect of EG and DPC is beyond the scope of this paper, which focuses on the description of the structural changes observed in the proteins.

The experimental strategy consisted of establishing the shape of the MCR components describing the spectra of the largest available protein set in the native structural state, called  $\text{D}_{192}$ . When applied to  $\text{D}_{185}$ , a subset of  $\text{D}_{192}$ , these components could describe the spectra well but, when applied to  $\text{D}_{285}$ , the LOF was more than doubled, indicating the presence of structures that did not exist in native proteins. An additional component, called here MCR-E3, could account for a significant fraction of the LOF increase. The shape of this new component indicates that it is an unusual  $\beta$ -sheet structure. In native proteins, the  $\beta$ -sheet structure has a spectral signature between 1630 and 1642  $\text{cm}^{-1}$ .<sup>17,51</sup> As reviewed elsewhere, the band near 1620  $\text{cm}^{-1}$  can be related to aggregated species and probably correspond to intermolecular  $\beta$  structure formation.<sup>21</sup> The MCR-E3 component was therefore assigned to intermolecular  $\beta$ -sheet.

### 3.1. Appearance of Intermolecular $\beta$ -Sheet Structure.

More than any other structural changes, the presence of intermolecular  $\beta$ -sheet is critical, in particular in the field of therapeutic proteins. Indeed, protein aggregates are a significant risk factor for deleterious immune responses in patients, including against the active protein monomer.<sup>1</sup> As reviewed by Roberts,<sup>1</sup> aggregates are usually irreversible but retain some fraction of their original folded structure, eliciting an immune response when compared to the parent monomer and resulting in antidrug antibodies (ADA).<sup>2</sup> Neutralizing the antibody can both inhibit the efficacy of the product and, cross-reactively, neutralize an endogenous protein counterpart and induce severe immediate hypersensitivity responses (e.g., anaphylaxis).<sup>52</sup> The appearance of intermolecular  $\beta$ -sheet bridging monomers in multimers was found in about 35% of

the proteins belonging to the  $\text{D}_{185}$  protein set tested. Figure 6 reports the content in the MCR-E3 component in 85 proteins

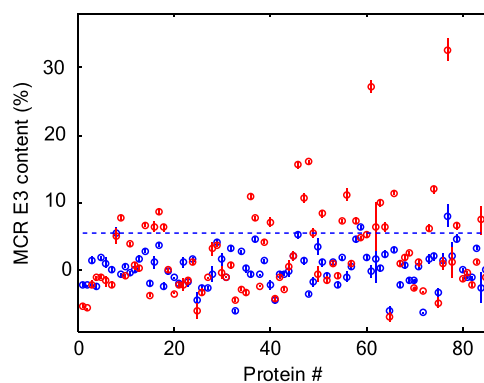


**Figure 6.** Content of the MCR-E3 component in  $\text{D}_{185}$  (blue circle) and  $\text{D}_{285}$  (red circle) data sets. Proteins numbered from 1 to 85 have been sorted in the  $\alpha$ -helix content, descending order. The vertical bar present in each symbol represents 2 standard deviations ( $n = 4$ ).

for  $\text{D}_{185}$  and  $\text{D}_{285}$  datasets. This content can be easily calculated for any set of spectra from the MCR profiles available in Table S4. It appears that for the native protein set ( $\text{D}_{185}$ ), only 2 proteins in MCR-E3 have content clearly above 5.5% while 25 proteins from  $\text{D}_{285}$  are clearly above this threshold. In Figure 6, proteins have been sorted in order of decreasing  $\alpha$ -helix content. Figure 6, therefore, indicates that the MCR-E3 content is randomly distributed with respect to the helix content in native proteins.

**3.2. Other Structural Changes.** Though aggregation may be the main concern for therapeutic proteins, other structural changes can occur during partial denaturation. Figure 7A reports the mean structural change in the 85 proteins. The largest changes appear as a loss of MCR-E2 and a gain of MCR-O2 components. The gain in the MCR-E3 component comes only in the third position. The mean change observed for MCR-H is relatively modest (Figure 7A) and the smallest with respect to its natural abundance in the  $\text{D}_{185}$  (Figure S4). With respect to its original contribution in  $\text{D}_{185}$ , MCR-E3 displays the largest relative change with a ca 200% increase (Figure S4).

**3.3. Correlations between Structural Changes.** Even though the present work is not intended to shed light on the mechanisms underlying the structural changes induced by incubation in the presence of DPC and EG, protein-by-protein analysis allows significant correlations between the changes to be evidenced. It raises the possibility to analyze the general trends in the transformation of one structure into another. Figure 7B reports the changes in the content of each MCR component for each protein. It can be used to examine whether some secondary structures are more prone to transformation into another one. The only feature that appears visually is that MCR-E1 increases in proteins with a high  $\alpha$ -helix content (say proteins #1–50) and decreases in proteins with low  $\alpha$ -helix content (say proteins #50–85) and conversely for MCR-E2. Yet, the correlation coefficients are only +0.39 and  $-0.38$ , respectively, though associated with  $P$ -values below 0.03% (Figure S5). Figure 8 illustrates the correlations between the changes in the MCR component contents induced by the experimental conditions used here. The numerical values of the correlation coefficients and the corresponding  $P$ -values can be found in Figure S5.

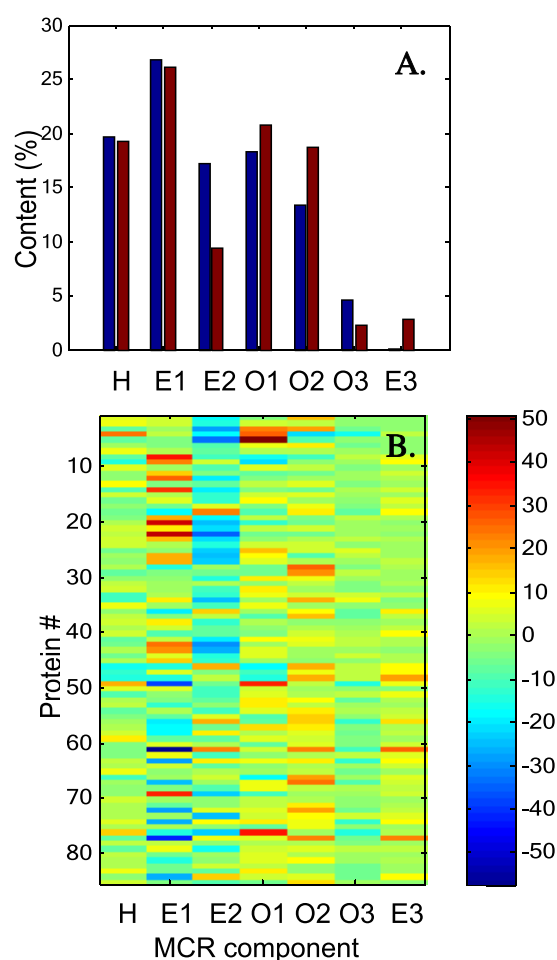


**Figure 7.** (A) Global content (mean over the 85 proteins) in the 7 MCR components for the native protein set (blue bars) and for the protein set exposed to EG and DPC (red bars). (B) Color-coded extent of the content change (content in  $D2_{85}$  - content in  $D1_{85}$ ) for each MCR component reported in the abscissa and for each protein numbered from 1 to 85 in the ordinate. Proteins are sorted in the order of decreasing  $\alpha$ -helix content.

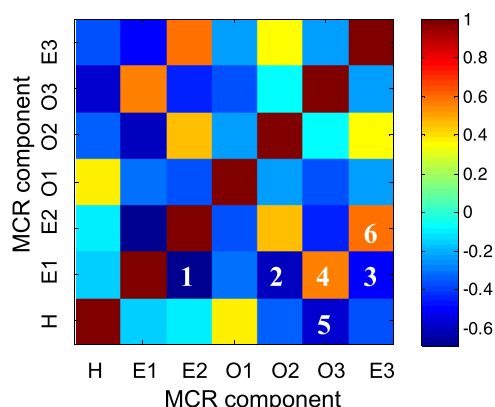


**Figure 8.** Color-coded correlation coefficient between the changes in the MCR component content upon exposure of the 85 proteins to DPC and EG. The color bar on the right indicates scaling. The numbered squares are the highest correlation values ( $|R| > 0.5$ ), as discussed in the text.

A few critical features potentially relevant for the mechanism of the structural changes can be obtained from Figure 8, where

the largest correlation values are identified by a label. The anticorrelation identified by labels 1, 2, and 3 indicates that the MCR-E1 content variations are anticorrelated to those of MCR-E2, MCR-O2, and MCR-E3. The correlation coefficients ( $R$ ) are, respectively,  $-0.69$ ,  $-0.59$ , and  $-0.50$ . The only positive correlation is with MCR-O3 ( $R = +0.57$ , label 4). For the  $\alpha$ -helix content, the only significant correlation is found with MCR-O3 ( $R = -0.58$ , label 5). Overall, the H structure loss is essentially transformed into MCR-O3, and the  $\beta$ -sheet structure MCR-E2 absorbing at  $1642\text{ cm}^{-1}$  is essentially transformed into MCR-E1 absorbing at  $1632\text{ cm}^{-1}$  ( $R = -0.69$ , label 1). MCR-E2 and MCR-E3 have a positive correlation ( $R = 0.59$ , label 6). Before any interpretation, it must be kept in mind that this is a global observation of each protein. Changes occurring within a protein and globally canceling each other cannot be investigated without a detailed analysis of the kinetics of the evolution of each of them, which was beyond the scope of the present work.

In conclusion, MCR provided 6 structurally meaningful components: 3 of them could be assigned to well-defined secondary structures and the other 3 were assigned to "Others", essentially representing the disordered fraction of the proteins. None of them could be clearly correlated with the DSSP-defined T, S, and B structures. Very interestingly, MCR-ALS could model a new component profile that appears only when proteins have been subjected to mild denaturing conditions. Comparison with the literature allowed the assignment of this component to the intermolecular  $\beta$ -sheet that links together protein molecules, resulting in protein aggregation. Semiquantitative evaluation of this new structure (Figure 6) is easily obtained by solving eq 1 for C. The necessary MCR components profiles  $S^T$  (Figure 5) are provided in Table S4.

## ■ ASSOCIATED CONTENT

### Supporting Information

The Supporting Information is available free of charge at <https://pubs.acs.org/doi/10.1021/acs.analchem.1c01416>.

Summary of protein preparation methods, microarray printing, imaging procedures and spectrum processing and analysis; spectral reproducibility (Figure S1); evolution of MCR parameters as a function of the number of components (Figure S2);  $D2_{85}$ - $D1_{85}$  differences (Figure S3); the correlation between structure content and structure changes (Figure S4); the correlation between the MCR component and secondary structure content (Figure S5); 4 tables reporting the standard deviation of structural elements; the correlation between the MCR component content and DSSP-defined structure content; the list of the proteins, and the 7 MCR components to be used to compute their content in any new protein spectrum (PDF)

## ■ AUTHOR INFORMATION

### Corresponding Author

Erik Goormaghtigh – Center for Structural Biology and Bioinformatics, Laboratory for the Structure and Function of Biological Membranes, Campus Plaine, Université Libre de Bruxelles CP206/2, B1050 Brussels, Belgium; [orcid.org/0000-0002-2071-2262](https://orcid.org/0000-0002-2071-2262); Email: [egoor@ulb.ac.be](mailto:egoor@ulb.ac.be)

## Author

Joëlle De Meutter – Center for Structural Biology and Bioinformatics, Laboratory for the Structure and Function of Biological Membranes, Campus Plaine, Université Libre de Bruxelles CP206/2, B1050 Brussels, Belgium

Complete contact information is available at:

<https://pubs.acs.org/10.1021/acs.analchem.1c01416>

## Funding

The manuscript was written through contributions of all authors. All authors have given approval to the final version of the manuscript.

## Notes

The authors declare no competing financial interest.

## ACKNOWLEDGMENTS

This work was supported by the Fonds de la Recherche Scientifique—FNRS under Grant no. O001518F (EOS-convention #30467715). The authors thank the INSTRUCT-ERIC European organization and the H2020 INFRAIA #101004806 MOSBRI project for supporting the protein microarrayer and FTIR imaging ROBOTTEIN platform. E.G. is Research Director with the National Fund for Scientific Research (Belgium).

## REFERENCES

- (1) Roberts, C. J. *Trends Biotechnol.* **2014**, *32*, 372–380.
- (2) Ratanji, K. D.; Derrick, J. P.; Dearman, R. J.; Kimber, I. J. *Immunotoxicol.* **2014**, *11*, 99–109.
- (3) Rosa, M.; Roberts, C. J.; Rodrigues, M. A. *PLoS One* **2017**, *12*, No. e0176748.
- (4) Ripple, D. C.; Dimitrova, M. N. *J. Pharm. Sci.* **2012**, *101*, 3568–3579.
- (5) Vázquez-Rey, M.; Lang, D. A. *Biotechnol. Bioeng.* **2011**, *108*, 1494–1508.
- (6) Tiernan, H.; Byrne, B.; Kazarian, S. G. *Spectrochim. Acta, Part A* **2020**, *241*, No. 118636.
- (7) Wilcox, K. E.; Blanch, E. W.; Doig, A. J. *Biochemistry* **2016**, *55*, 3794–3802.
- (8) De Meutter, J.; Goormaghtigh, E. *Anal. Chem.* **2021**, *93*, 3733–3741.
- (9) Goormaghtigh, E.; Ruyschaert, J. M.; Raussens, V. *Biophys. J.* **2006**, *90*, 2946–2957.
- (10) Cerf, E.; Sarroukh, R.; Tamamizu-Kato, S.; Breydo, L.; Derclaye, S.; Dufrene, Y. F.; Narayanaswami, V.; Goormaghtigh, E.; Ruyschaert, J. M.; Raussens, V. *Biochem. J.* **2009**, *421*, 415–423.
- (11) Celej, M. S.; Sarroukh, R.; Goormaghtigh, E.; Fidelio, G.; Ruyschaert, J. M.; Raussens, V. *Biochem. J.* **2012**, *443*, 719–726.
- (12) Zandomeneghi, G.; Krebs, M. R. H.; McCammon, M. G.; Fändrich, M. *Protein Sci.* **2004**, *13*, 3314–3321.
- (13) Shivu, B.; Seshadri, S.; Li, J.; Oberg, K. A.; Uversky, V. N.; Fink, A. L. *Biochemistry* **2013**, *52*, 5176–5183.
- (14) Dong, A.; Matsuura, J.; Manning, M. C.; Carpenter, J. F. *Arch. Biochem. Biophys.* **1998**, *355*, 275–281.
- (15) Dong, A.; Prestrelski, S. J.; Allison, S. D.; Carpenter, J. F. *J. Pharm. Sci.* **1995**, *84*, 415–424.
- (16) Seshadri, S.; Khurana, R.; Fink, A. L. *Methods Enzymol.* **1999**, *309*, 559–576.
- (17) Arrondo, J. L. R.; Goni, F. M. *Prog. Biophys. Mol. Biol.* **1999**, *72*, 367–405.
- (18) Baird, G.; Farrell, C.; Cheung, J.; Semple, A.; Blue, J.; Ahl, P. L. *Protein J.* **2020**, *39*, 318–327.
- (19) Devi, V. S.; Coleman, D. R.; Truntzer, J. *Protein J.* **2011**, *30*, 395–403.
- (20) Militello, V.; Casarino, C.; Emanuele, A.; Giostra, A.; Pullara, F.; Leone, M. *Biophys. Chem.* **2004**, *107*, 175–187.
- (21) Boulet-Audet, M.; Byrne, B.; Kazarian, S. G. *Anal. Chem.* **2014**, *86*, 9786–9793.
- (22) De Meutter, J.; Derfoufi, M. K.; Goormaghtigh, E. *Biomed. Spectrosc. Imaging* **2016**, *5*, 145–154.
- (23) De Meutter, J.; Vandenameele, J.; Matagne, A.; Goormaghtigh, E. *Analyst* **2017**, *142*, 1371–1380.
- (24) De Meutter, J.; Goormaghtigh, E. *Eur. Biophys. J.* **2021**, *50*, 613–628.
- (25) De Meutter, J.; Goormaghtigh, E. *Anal. Chem.* **2021**, *93*, 1561–1568.
- (26) De Meutter, J.; Goormaghtigh, E. *Eur. Biophys. J.* **2021**, *50*, 641–651.
- (27) De Meutter, J.; Goormaghtigh, E. *Comput. Struct. Biotechnol. J.* **2020**, *18*, 1864–1876.
- (28) De Juan, A.; Jaumot, J.; Tauler, R. *Anal. Methods* **2014**, *6*, 4964–4976.
- (29) Ruckebusch, C.; Blanchet, L. *Anal. Chim. Acta* **2013**, *765*, 28–36.
- (30) Perez-Guaita, D.; Quintas, G.; Farhane, Z.; Tauler, R.; Byrne, H. J. *Talanta* **2020**, *208*, No. 120386.
- (31) de Juan, A.; Tauler, R. *Anal. Chim. Acta* **2021**, *1145*, 59–78.
- (32) Mendieta, J.; Díaz-Cruz, M. S.; Esteban, M.; Tauler, R. *Biophys. J.* **1998**, *74*, 2876–2888.
- (33) Alcaráz, M. R.; Schwaighofer, A.; Goicoechea, H.; Lendl, B. *Spectrochim. Acta, Part A* **2017**, *185*, 304–309.
- (34) Shariati-Rad, M.; Hasani, M. *Biochimie* **2009**, *91*, 850–856.
- (35) Tauler, R. *Chemom. Intell. Lab. Syst.* **1995**, *30*, 133–146.
- (36) Jaumot, J.; Juan, A.; De; Tauler, R. *Chemom. Intell. Lab. Syst.* **2015**, *140*, 1–12.
- (37) Windig, W. *Chemom. Intell. Lab. Syst.* **1997**, *36*, 3–16.
- (38) Windig, W.; Antalek, B.; Lippert, J. L.; Batonneau, Y.; Brémard, C. *Anal. Chem.* **2002**, *74*, 1371–1379.
- (39) Barth, A. *Biochim. Biophys. Acta, Bioenerg.* **2007**, *1767*, 1073–1101.
- (40) Nevskaya, N. A.; Chirgadze, Y. N. *Biopolymers* **1976**, *15*, 637–648.
- (41) Goormaghtigh, E.; Cabiaux, V.; Ruyschaert, J. M. *Subcell. Biochem.* **1994**, *23*, 329–362.
- (42) Chirgadze, Y. N.; Nevskaya, N. A. *Biopolymers* **1976**, *15*, 627–636.
- (43) Goormaghtigh, E.; Cabiaux, V.; Ruyschaert, J. M. *Subcell. Biochem.* **1994**, *23*, 405–450.
- (44) Bernstein, F. C.; Koetzle, T. F.; Williams, G. J.; Meyer, E. F.; Brice, M. D.; Rodgers, J. R.; Kennard, O.; Shimanouchi, T.; Tasumi, M. *J. Mol. Biol.* **1977**, *112*, 535–542.
- (45) Kabsch, W.; Sander, S. *Biopolymers* **1983**, *22*, 2577–2637.
- (46) Arrondo, J. L.; Muga, A.; Castresana, J.; Goñi, F. M. *Prog. Biophys. Mol. Biol.* **1993**, *59*, 23–56.
- (47) Wolpert, M.; Hellwig, P. *Spectrochim. Acta, Part A* **2006**, *64*, 987–1001.
- (48) Rahmelow, K.; Hubner, W.; Ackermann, T. *Anal. Biochem.* **1998**, *257*, 1–11.
- (49) Oberg, K. A.; Ruyschaert, J. M.; Goormaghtigh, E. *Eur. J. Biochem.* **2004**, *271*, 2937–2948.
- (50) Kurauskas, V.; Hessel, A.; Ma, P.; Lunetti, P.; Weinhäupl, K.; Imbert, L.; Brutscher, B.; King, M. S.; Sounier, R.; Dolce, V.; Kunji, E. R. S.; Capobianco, L.; Chipot, C.; Dehez, F.; Bersch, B.; Schanda, P. *J. Phys. Chem. Lett.* **2018**, *9*, 933–938.
- (51) Sarroukh, R.; Goormaghtigh, E.; Ruyschaert, J.-M.; Raussens, V. *Biochim. Biophys. Acta, Biomembr.* **2013**, *1828*, 2328–2338.
- (52) Rosenberg, A. S. *AAPS J.* **2006**, *8*, E501–E507.